

# Unsupervised clustering algorithm for efficient processing of 4D-STEM and 5D-STEM data

**Serin Lee,<sup>1,\*</sup> Stephanie M. Ribet,<sup>2</sup> Arthur R. C. McCray,<sup>1</sup> Andrew Barnum,<sup>3</sup> Jennifer A. Dionne<sup>1,\*</sup> and Colin Ophus<sup>1,\*</sup>**

<sup>1</sup>Department of Materials Science and Engineering, Stanford University, Stanford, 94305, CA, United States,

<sup>2</sup>National Center for Electron Microscopy, Molecular Foundry, Lawrence Berkeley National Laboratory, Berkeley, 94720, CA, United States and <sup>3</sup>Stanford Nano Shared Facilities, Stanford University, Stanford, 94305, CA, United States

\*Corresponding author. [serinl@stanford.edu](mailto:serinl@stanford.edu), [jdionne@stanford.edu](mailto:jdionne@stanford.edu), [cophus@stanford.edu](mailto:cophus@stanford.edu)

FOR PUBLISHER ONLY Received on Date Month Year; revised on Date Month Year; accepted on Date Month Year

## Abstract

Four-dimensional scanning transmission electron microscopy (4D-STEM) enables mapping of diffraction information with nanometer-scale spatial resolution, offering detailed insight into local structure, orientation, and strain. However, as data dimensionality and sampling density increase, particularly for *in situ* scanning diffraction experiments (5D-STEM), robust segmentation of spatially coherent regions becomes essential for efficient and physically meaningful analysis. Here, we introduce a clustering framework that identifies crystallographically distinct domains from 4D-STEM datasets. By using local diffraction-pattern similarity as a metric, the method extracts closed contours delineating regions of coherent structural behavior. This approach produces cluster-averaged diffraction patterns that improve signal-to-noise and reduce data volume by orders of magnitude, enabling rapid and accurate orientation, phase, and strain mapping. We demonstrate the applicability of this approach to *in situ* liquid-cell 4D-STEM data of gold nanoparticle growth. Our method provides a scalable and generalizable route for spatially coherent segmentation, data compression, and quantitative structure–strain mapping across diverse 4D-STEM modalities. The full analysis code and example workflows are publicly available to support reproducibility and reuse.

**Key words:** clustering, 4D-STEM, 5D-STEM, strain, orientation

## Introduction

Advances in four-dimensional scanning transmission electron microscopy (4D-STEM) now allow mapping of diffraction information with nanometer resolution [Ophus, 2019]. Each probe position records a diffraction pattern, giving a spatially resolved view of local structure, strain, and orientation. Unlike selected-area and micro-diffraction, which average over micrometer-scale regions, the scanning nanobeam mode captures diffraction from a probe orders of magnitude smaller, revealing nanoscale structural variations that conventional methods cannot access. Previous studies have shown how automated crystal orientation mapping (ACOM), namely template matching of diffraction pattern libraries on 4D-STEM datasets allows crystal orientation mapping including through open-source code frameworks [Rauch et al., 2010, Ophus et al., 2022, Cautaerts et al., 2022].

However, traditional analyses of the 4D-STEM datasets often rely on manually selected regions of interest or global thresholding to separate diffraction signals. These approaches can overlook

subtle but physically meaningful variations across neighboring probe positions, especially in samples composed of closely spaced nanocrystals or partially coherent domains [Mahr et al., 2021, Saha et al., 2025]. Recent studies have employed unsupervised clustering methods, such as K-means clustering [Liu et al., 2024, Kim et al., 2025], non-negative matrix factorization [Uesugi et al., 2021, Allen et al., 2021, Kimoto et al., 2025], and hierarchical clustering [Kimoto et al., 2024] on 4D-STEM datasets, to identify regions with similar diffraction signatures. There are also approaches on segmenting and clustering 4D-STEM datasets through machine learning workflow, such as by using Gaussian mixture models [Liu et al., 2025] and using variational autoencoders [Kho et al., 2025]. While these techniques can reveal meaningful structural trends, they are sensitive to many user-specified parameters and therefore difficult to apply to varied datasets. As a result, they may struggle to capture irregularly shaped or hierarchically nested regions, which are common in polycrystalline or beam-sensitive

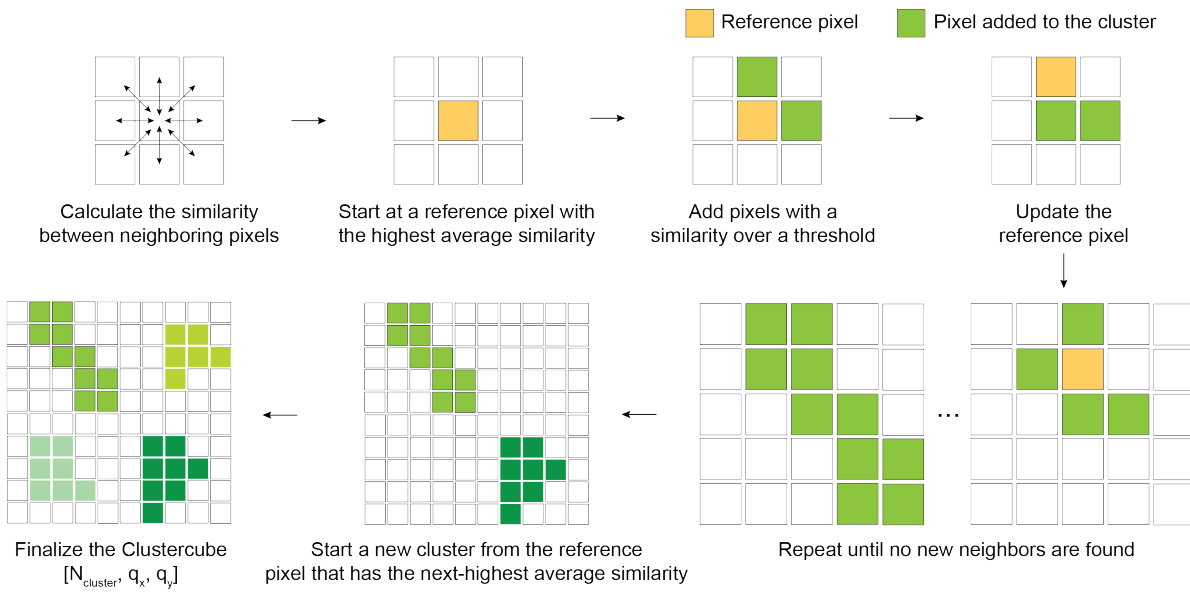


Fig. 1: Schematic of the clustering process based on marching-square algorithm.

systems. Moreover they are not embedded in open-source code pipelines, creating additional steps for data processing.

Modern detectors exacerbate these problems by enabling fast, high-resolution, low-dose measurements, conditions that often yield diffraction patterns with low signal-to-noise ratios. These innovations have heightened the need for robust and reliable clustering methods for interpreting the resulting high-dimensional data [Roccapriore et al., 2022]. Moreover, the massive size of 4D-STEM datasets demands computational methods that extract representative information while compressing the data without losing structural detail [Kimoto et al., 2024]. This challenge becomes even more pronounced for *in situ* 4D-STEM, i.e. 5D-STEM experiments [Miller et al., 2024], where datasets are accumulated over time, effectively adding a temporal dimension to the already large four-dimensional data structure [Pekin et al., 2019, Miller et al., 2023, da Silva et al., 2022, Winkler et al., 2024, Miller et al., 2025a, Chen et al., 2025]. Computationally efficient and physically meaningful interpretation is therefore indispensable for the resulting large data volumes. Furthermore, 5D-STEM experiments can often involve complex environments near the sample such as liquid or gas cells [Liu et al., 2024, Sun et al., 2024, Miller et al., 2025b, Cheng et al., 2025, Patrick et al., 2025]. The additional thickness associated with these experimental set-ups can degrade signal-to-noise ratios, making reliable segmentation and data reduction even more critical for quantitative analysis.

Here, we present a clustering framework based on the marching squares algorithm to automatically segment spatially coherent features within 4D-STEM datasets. By treating similarity maps between diffraction patterns as the metric to define clusters, our method extracts closed contours that trace the boundaries of crystallographically distinct regions. This approach provides a generalizable and computationally efficient means of identifying nanoscale domains, enabling researchers to analyze diffraction signals from regions that yield the most physically meaningful information. In addition to segmentation, the method reduces the real-space dimension from the total number of probes

to the number of clusters (typically on the order of  $10^{-2} - 10^{-3}$ ), producing a single representative diffraction pattern for each cluster. Averaging diffraction patterns within each cluster enhances the signal-to-noise ratio and facilitates downstream analysis such as orientation mapping, strain measurement, and structure determination. This combination of spatial segmentation, data reduction, and signal enhancement establishes a scalable workflow for interpreting large 4D-STEM datasets. To ensure broad applicability, the framework is designed as a versatile tool with only a few user-tunable parameters, allowing easy adaptation to diverse datasets, and also implemented as a module in the open-source Python package `py4DSTEM`.

## Methods

### Clustering of 4D-STEM Data

To identify spatially coherent regions exhibiting similar diffraction behavior, we developed a marching-square-based clustering algorithm that segments 4D-STEM data based on local correlation of diffraction patterns. The algorithm operates in three stages: (i) computation of a pixel-wise similarity matrix, (ii) real-space background masking and thresholding, (iii) recursive clustering using a fixed neighbor search array, and (iv) refining cluster and averaging diffraction cubes (Fig. 1).

#### 1. Similarity Matrix Calculation

Each 4D-STEM dataset  $D(r_x, r_y, q_x, q_y)$  is treated as a two-dimensional array of diffraction patterns indexed by probe positions  $(x, y)$ . For each probe position, the diffraction pattern  $I_{x,y}(q_x, q_y)$  is optionally Gaussian-blurred with a kernel width of  $\sigma = 3$  to reduce high-frequency noise (an additional correlative filtering step is applied and discussed later).

To restrict the similarity calculation to a desired reciprocal-space region, a diffraction-space mask  $M_q(q_x, q_y)$  can be applied:

$$I'_{x,y}(q_x, q_y) = I_{x,y}(q_x, q_y) \cdot M_q(q_x, q_y)$$

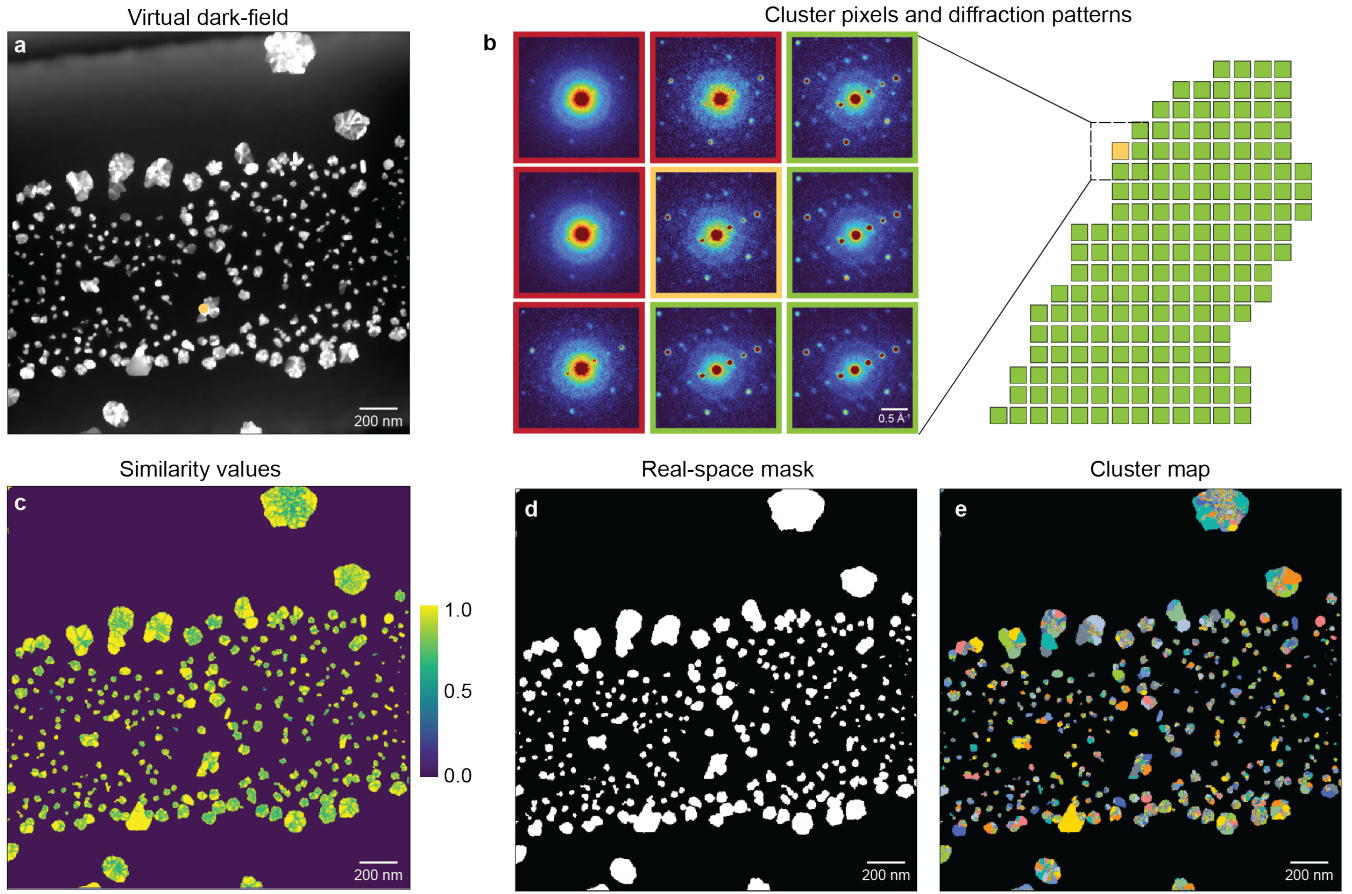


Fig. 2: Applying clustering to the 4D-STEM dataset. a. Virtual dark field image of the Au nanoparticles formed by the electron-beam induced reduction of Au cation precursors. b. (left) Diffraction pattern from the reference pixel (yellow box; marked as the yellow dot in panel a). Neighboring pixels with diffraction patterns above the similarity threshold are highlighted in green, while those below the threshold are shown in red. (right) Schematic illustration of the resulting cluster, where each square corresponds to a probe position within the cluster. c. Plot of the similarity values ( $\bar{S}(x, y)$ ), where the color range spans from 0 to 1. d. Real-space mask generated for the background thresholding. e. Cluster map, where colors were iterated over ten distinct color codes to differentiate clusters.

The similarity ( $S(x, y, \Delta)$ ) between each diffraction pattern and its neighbors is computed using a normalized cosine correlation:

$$S(x, y, \Delta) = \frac{\sum_{q_x, q_y} I'_{x, y}(q_x, q_y) I'_{x+\Delta_x, y+\Delta_y}(q_x, q_y)}{\sqrt{\sum_{q_x, q_y} I'_{x, y}(q_x, q_y)^2} \sqrt{\sum_{q_x, q_y} I'_{x+\Delta_x, y+\Delta_y}(q_x, q_y)^2}}$$

Here,

$$\Delta = \{(-1, -1), (-1, 0), (-1, 1), (0, -1), (0, 1), (1, -1), (1, 0), (1, 1)\}$$

represents the eight fixed nearest-neighbor offsets used in the marching-square scheme. The resulting 3D similarity array  $S(x, y, n)$  stores one similarity value per neighbor direction  $n$ .

## 2. Real-Space Masking and Background Thresholding

To suppress background regions with low signal or outside the area of interest and reduce computational cost, the similarity values are first averaged over all neighbor directions to obtain a scalar map:

$$\bar{S}(x, y) = \frac{1}{N} \sum_{n=1}^N S(x, y, n)$$

where  $N = 8$  represents the number of neighbor directions. A real-space mask  $M_r(x, y)$  is then applied to this averaged similarity map to exclude non-sample or low-signal regions:

$$\bar{S}'(x, y) = \bar{S}(x, y) \cdot M_r(x, y)$$

Pixels outside the mask (i.e.  $M_r = 0$ ) are excluded from further analysis.

## 3. Marching-Square Clustering

Clustering proceeds by iteratively growing connected regions whose local similarity exceeds a predefined threshold. The process begins from the unassigned pixel with the highest  $\bar{S}(x, y)$ , which serves as the seed of a new cluster. From this seed, the algorithm inspects its eight neighboring pixels defined by  $\Delta$ . A neighbor  $(x + \Delta_x, y + \Delta_y)$  is added to the cluster if

$$S'(x, y, \Delta) \geq T$$

where  $T$  is the user-defined similarity threshold, and if the neighbor has not already been assigned to another cluster. Each accepted pixel becomes a new node for expansion, forming a

recursive marching loop until no new neighboring pixels satisfy the threshold. When cluster growth halts, the current region is finalized, and the next unassigned pixel with the highest remaining  $\bar{S}(x, y)$  is used to seed a new cluster. This process repeats until all pixels are either assigned to a cluster or masked out.

#### 4. Cluster Refinement and Averaged Diffraction Cubes

Each resulting cluster  $C_i$  contains the real-space coordinates of its member pixels, where  $i$  refers to cluster number. To suppress noise-induced fragments, clusters smaller than a specified minimum size can be excluded. For each remaining cluster, an averaged diffraction pattern is generated:

$$I_{C_i} = \frac{1}{|C_i|} \sum_{(x, y) \in C_i} I_{x, y}(q_x, q_y)$$

This produces a reduced cluster-averaged diffraction cube representing the mean diffraction behavior of each region, which now reduces the data from  $D(x, y, q_x, q_y)$  to a 3D representation of  $D(N_{\text{cluster}}, q_x, q_y)$ .

#### Correlative Prefiltering of the 4D-STEM dataset

To enhance the local signal-to-noise ratio and suppress spurious noise before clustering, a correlative filtering procedure was applied to the dataset that is Gaussian-blurred in the reciprocal space, using a similar method that has been previously reported and demonstrated [Chen and Kuo, 2010, Stangebye et al., 2025]. For each probe position  $(x, y)$ , the blurred diffraction pattern  $I_{x, y}(q_x, q_y)$  was compared with its neighboring patterns within a predefined offset range  $\{(\Delta x_i, \Delta y_i)\}$ . This step produces a locally averaged dataset that preserves the spatial coherence of correlated features while minimizing uncorrelated background fluctuations.

A spatial weight function  $w(q_x, q_y)$  was defined to emphasize the central region of each diffraction pattern while suppressing the contribution of high-angle scattering and edge artifacts. The weight was constructed as a normalized radial function:

$$w(q_x, q_y) = \left[ \frac{\sqrt{(q_x - \bar{q}_x)^2 + (q_y - \bar{q}_y)^2}}{\sqrt{N_{q_x} N_{q_y}}} \right]^2$$

where  $(\bar{q}_x, \bar{q}_y)$  denote the mean in the reciprocal space, and  $N_{q_x}, N_{q_y}$  are the diffraction pattern dimensions.

Each diffraction pattern was then weighted and normalized. The weighted mean intensity was subtracted, and the pattern was normalized by its L2 norm:

$$\tilde{I}_{x, y} = \frac{\left( I_{x, y} - \frac{\sum I_{x, y} w}{\sum w} \right) w}{\sqrt{\sum \tilde{I}_{x, y}^2}}$$

The correlation coefficient ( $R_i$ ) between the reference pixel  $(x, y)$  and each neighboring pixel  $(x + \Delta x_i, y + \Delta y_i)$  was computed as:

$$R_i(x, y) = \sum_{q_x, q_y} \tilde{I}_{x, y}(q_x, q_y) \tilde{I}_{x + \Delta x_i, y + \Delta y_i}(q_x, q_y)$$

The neighbor offsets  $(\Delta x_i, \Delta y_i)$  were defined within a circular *footprint* of radius  $r = 4$ , corresponding to 81 neighboring probe positions.

The correlation values were mapped into a normalized range  $[0, 1]$  using a predefined correlation range  $(R_{\min}, R_{\max}) = (0.85, 0.95)$ :

$$\hat{R}_i = \text{clip} \left( \frac{R_i - R_{\min}}{R_{\max} - R_{\min}}, 0, 1 \right)$$

Finally, the intensity at each probe position was refined by weighted accumulation of its neighboring patterns according to their correlation strength:

$$I'_{x, y} = \frac{I_{x, y} + \sum_i \hat{R}_i I_{x + \Delta x_i, y + \Delta y_i}}{\sum_i \hat{R}_i}$$

This filtering process effectively averages each diffraction pattern with its correlated neighbors while preventing over-smoothing across distinct regions. The resulting filtered dataset was subsequently used for similarity calculation and marching-square clustering.

#### 4D-STEM experiment

As a model system to demonstrate the clustering of the 4D-STEM dataset, we used Au nanoparticles grown by the electron-beam induced radiolysis in liquid cell TEM [Woehl et al., 2012, Schneider et al., 2014, Woehl et al., 2020, Lee et al., 2023, Fritsch et al., 2025, Lee et al., 2024]. We introduce aqueous 1mM HAuCl<sub>4</sub> solution into a liquid-cell holder (Insight Chips, Flow-holder) with a 80 nm-thick channel (Insight Chips, Nano Channel Chips), and the Au nanoparticles were grown under the electron beam irradiation with an electron flux of  $1.14 \text{ e}^- \text{ \AA}^{-2} \text{ s}^{-1}$ . The left panel of the Fig. 2a shows the virtual dark-field image of the Au nanocrystals formed after a total 45 s of irradiation. The 4D-STEM data was collected on a Thermo-Fisher probe-corrected Spectra microscope. The 4D-STEM time series data was collected on the Dectris Arina camera with a frame size of  $512 \times 512$ , convergence angle of 0.622 mrad, and a dwell time of  $50 \mu\text{s}$  per probe position [Stroppa et al., 2023].

The yellow-boxed image of the right panel of the Fig. 2a shows the reference pixel of the first cluster, and the green-boxed images show the neighboring pixels that were added to the cluster since they had a similarity higher than the threshold (0.9 in the example). Fig. 2b shows the diffraction patterns of the first 30 pixels that were added to the cluster during the iterative process. To apply the marching-square clustering, first the  $S(x, y)$  was calculated (Fig. 2c). The background was thresholded using the triangle method [Van der Walt et al., 2014] to produce the real-space mask (Fig. 2d). We then applied our clustering algorithm, and the resulting clusters are shown in Fig. 2d.

#### Orientation and Strain mapping

The clustered datacube was used to calculate orientation and strain maps using the workflows with ACOM [Ophus et al., 2022] from py4DSTEM package [Savitzky et al., 2021]. Note that depending on the experiment, filtering or preprocessing to remove the descan can be performed to improve the matching.

## Results

We first compare diffraction patterns from the same probe positions before and after applying the clustering algorithm. In the virtual dark-field image (Fig. 3a), the colored markers denote the seed pixels, which are defined as the first reference pixel of

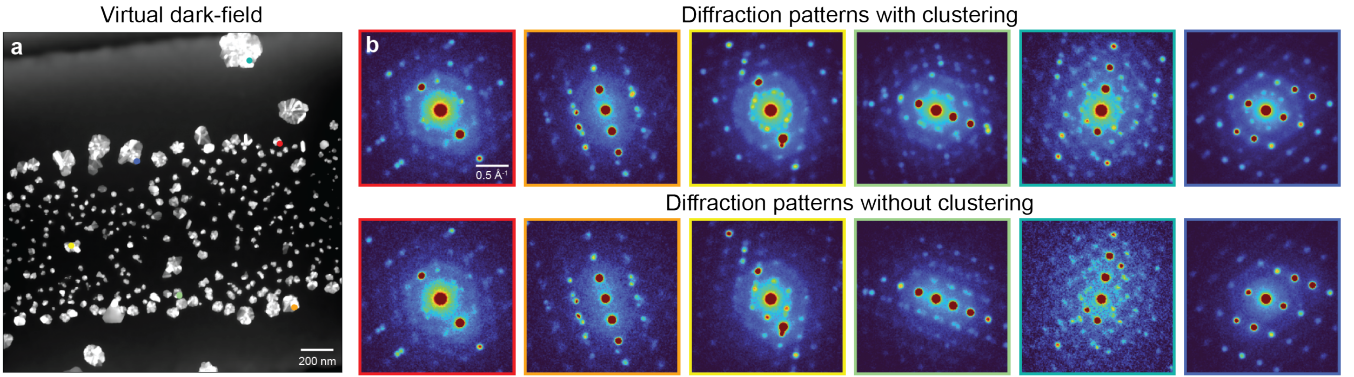


Fig. 3: Comparing diffraction patterns with and without clustering. (a) Virtual dark-field image with colored markers indicating the six cluster seeds. (b) Diffraction patterns from the same positions with clustering (top) and without clustering (bottom).

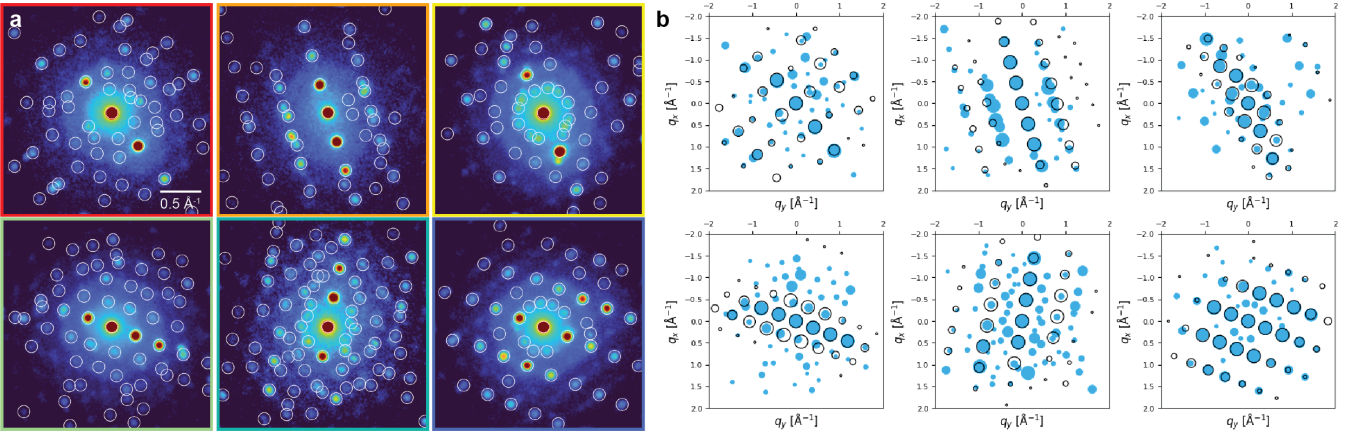


Fig. 4: Bragg disk detection with clustering. Bragg disk detector (a) and orientation mapping by ACOM template matching (b) on diffraction patterns.

each of the six identified clusters. The corresponding averaged diffraction patterns for each cluster are displayed in the top row of Fig. 3b. For comparison, the bottom row shows the raw diffraction patterns at the same seed pixel positions prior to clustering. Fig. S1 shows the diffraction patterns prior to clustering and also prefiltering. The clustered averages exhibit a markedly improved signal-to-noise ratio, enhancing the visibility of diffraction features, particularly at higher scattering angles, and thereby demonstrating the effectiveness of clustering in recovering weak high-angle signals.

We next perform the ACOM analysis on the clustered dataset. Fig. 4a presents representative clustered diffraction patterns overlaid with detected Bragg disks used for parameter tuning, while Fig. 4b shows examples of ACOM template matches. The clustering substantially improves computational efficiency in the Bragg disk matching step. Without clustering, matching must be performed for every probe position, corresponding to  $N_{\text{probe}} = 512 \times 512 = 2.62 \times 10^5$  diffraction patterns. With clustering, matching is instead carried out once per cluster, reducing the total operations to  $N_{\text{cluster}}$ . The resulting computational cost scales as

$$R = \frac{N_{\text{cluster}}}{N_{\text{probe}}},$$

where  $R \ll 1$ , typically on the order of  $10^{-2} - 10^{-3}$  depending on the dataset. This reduction by several orders of magnitude enables rapid and scalable orientation mapping while maintaining accuracy in the ACOM results. Moreover, compared to the ACOM analysis on dataset without clustering (Fig. S2a,b) and the raw dataset without clustering and prefiltering (Fig. S2c,d), clustering detects higher scattering angle bragg disks along with less overlapping.

We subsequently perform orientation and strain mapping, as summarized in Figure 5. Both the in-plane (left, Fig. 5a) and out-of-plane (middle, Fig. 5a) orientations are determined using the conventional ACOM workflow, with the mapping performed by assigning to each real-space position the orientation of its corresponding cluster.

For strain analysis, we introduce a physically consistent approach that leverages both clustered and non-clustered Bragg peak information (middle, Fig. 5a). From ACOM maps, the strain at each position can be calculated by comparing to the reference cif file as described in [Ribet et al., 2025]. To apply this to clustered data, the orientation map obtained after clustering is used as a reference lattice orientation, while the Bragg peak positions extracted from the non-clustered diffraction patterns are used to quantify local lattice distortions. Compared to the

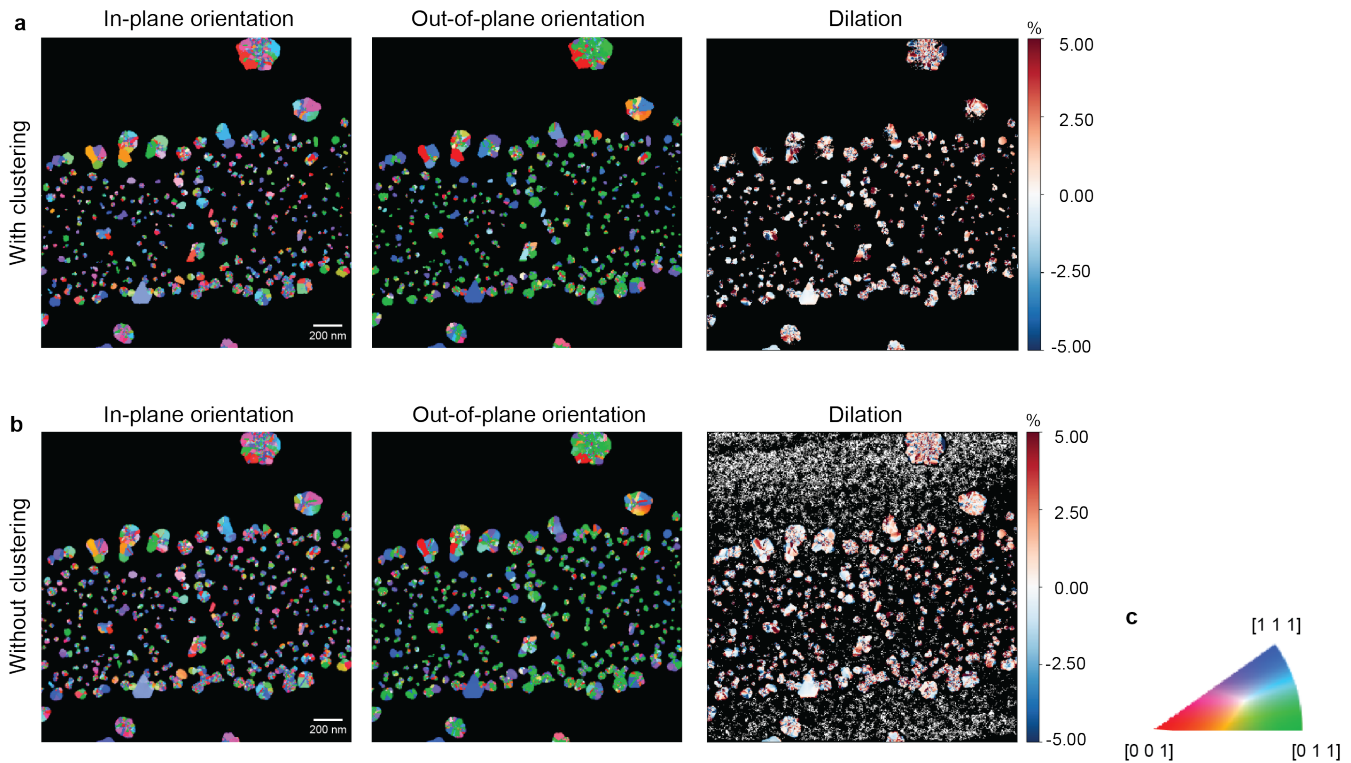


Fig. 5: Orientation and strain mapping with (a) and without clustering (b). a. (left) In-plane orientation map, (middle) out-of-plane orientation map, and (right) dilation map of a clustered dataset. b. (left) In-plane orientation map, (middle) out-of-plane orientation map, and (right) dilation map of a non-clustered dataset. c. Color legend of the orientation maps.

ACOM analysis on the non-clustered dataset (Fig. 5b), this hybrid analysis enables the extraction of spatially resolved strain fields with improved physical fidelity, revealing gradual strain variations across individual grains and at cluster boundaries.

## Discussion

The marching-square-based clustering framework offers a fast and generalizable route for identifying spatially coherent regions in 4D-STEM data. While it reduces the computational time, it also improves matches with higher order scattering angles by averaging over mistilt and mosaicity within the grain [Vincent and Midgley, 1994]. However, it also has limitations to be resolved. The algorithm assumes that each probe position is dominated by a well-defined diffraction pattern representative of a unique local structure. In cases where multiple crystalline domains overlap within the probe size, such as in areas with vertically stacked grains, the local diffraction signals become mixed, resulting in ambiguous similarity metrics and unstable cluster boundaries.

Despite these limitations, the proposed method offers significant practical advantages for processing 4D-STEM datasets. Implemented as an open-source user-friendly module within the py4DSTEM ecosystem, the algorithm requires only a few tunable parameters, primarily the similarity threshold and minimum cluster size, making it broadly accessible to users with varying computational backgrounds. A major advantage of this framework is the substantial reduction in effective data size, which greatly facilitates data handling, visualization, and storage. This

benefit becomes even more pronounced in *in situ* 4D-STEM (or 5D-STEM) experiments, where continuous acquisition rapidly produces massive datasets. Moreover, the low computational cost enables efficient processing even on standard CPUs, eliminating the need for specialized hardware. Together, these features establish a scalable and practical workflow for multidimensional electron microscopy analysis.

## Conclusion

We have developed a clustering algorithm for spatially coherent segmentation of 4D-STEM datasets. By defining local similarity between diffraction patterns and recursively tracing connected regions above a threshold, the method isolates nanoscale domains that exhibit consistent crystallographic behavior. This clustering enhances diffraction signal quality through regional averaging and reduces the computational load of subsequent analyses such as phase, orientation, and strain mapping by a significant amount, up to several orders of magnitude. The resulting cluster-averaged diffraction cubes enable efficient and physically interpretable quantification of orientation and strain, bridging the gap between raw multidimensional datasets and meaningful structural descriptors. Applied to *in situ* 4D-STEM of Au nanocrystals grown under electron irradiation, the approach robustly delineates grain boundaries and strain gradients even in noisy liquid-cell environments. More broadly, this framework offers a scalable foundation for real-time segmentation, data reduction,

and correlation analysis in next-generation multidimensional electron microscopy.

## Competing interests

No competing interest is declared.

## Data availability

The 4D-STEM dataset of the Au nanoparticle in the liquid cell TEM is available online. (<https://zenodo.org/records/18167694>) The analysis code is part of py4DSTEM (<https://github.com/py4dstem/py4DSTEM.git>), and the example Jupyter Notebook is in py4DSTEM\_tutorials repository ([https://github.com/py4dstem/py4DSTEM\\_tutorials](https://github.com/py4dstem/py4DSTEM_tutorials)).

## Acknowledgments

S.L. and J.A.D. acknowledge financial support from the Office of Basic Energy Sciences, U.S. Department of Energy, Division of Materials Science and Engineering, DE-AC02-76SF00515. Work at the Molecular Foundry was supported by the Office of Science, Office of Basic Energy Sciences, of the U.S. Department of Energy under Contract No. DE-AC02-05CH11231. The authors thank Professor Josh Kacher for helpful suggestions on the noisy diffraction pattern analysis. The authors thank Dr. Parivash Moradifar for the helpful discussions related to this work.

## References

Colin Ophus. Four-dimensional scanning transmission electron microscopy (4d-stem): From scanning nanodiffraction to ptychography and beyond. *Microscopy and Microanalysis*, 25(3):563–582, 2019.

Edgar F Rauch, Joaquin Portillo, Stavros Nicolopoulos, Daniel Bultreys, Sergei Rouvimov, and Peter Moeck. Automated nanocrystal orientation and phase mapping in the transmission electron microscope on the basis of precession electron diffraction. *Zeitschrift für Kristallographie*, 225(2-3):103–109, 2010.

Colin Ophus, Steven E Zeltmann, Alexandra Bruefach, Alexander Rakowski, Benjamin H Savitzky, Andrew M Minor, and Mary C Scott. Automated crystal orientation mapping in py4dstem using sparse correlation matching. *Microscopy and microanalysis*, 28(2):390–403, 2022.

Niels Cautaerts, Phillip Crout, Håkon W Ånes, Eric Prestat, Jiwon Jeong, Gerhard Dehm, and Christian H Liebscher. Free, flexible and fast: Orientation mapping using the multi-core and GPU-accelerated template matching capabilities in the python-based open source 4D-STEM analysis toolbox pyxem. *Ultramicroscopy*, 237:113517, 2022.

Christoph Mahr, Knut Müller-Caspary, Tim Grieb, Florian F Krause, Marco Schowalter, and Andreas Rosenauer. Accurate measurement of strain at interfaces in 4d-stem: A comparison of various methods. *Ultramicroscopy*, 221:113196, 2021.

Ambarneil Saha, Alexander J Pattison, Karen C Bustillo, David W Mittan-Moreau, Aaron S Brewster, Jian Zhang, and Peter Ercius. Reuniting crystallography with real space: Ab initio structure elucidation with 4d-stem. *Proceedings of the National Academy of Sciences*, 122(42):e2508185122, 2025.

Chang Liu, Oliver Lin, Saran Pidaparthi, Haoyang Ni, Zhiheng Lyu, Jian-Min Zuo, and Qian Chen. 4d-stem mapping of nanocrystal reaction dynamics and heterogeneity in a graphene liquid cell. *Nano letters*, 24(13):3890–3897, 2024.

Sungin Kim, Valentin Briega-Martos, Shikai Liu, Kwanghwi Je, Chuqiao Shi, Katherine Marusak Stephens, Steven E Zeltmann, Zhijing Zhang, Rafael Guzman-Soriano, Wenqi Li, et al. Operando heating and cooling electrochemical 4d-stem probing nanoscale dynamics at solid–liquid interfaces. *Journal of the American Chemical Society*, 2025.

Fumihiko Uesugi, Shogo Koshiya, Jun Kikkawa, Takuro Nagai, Kazutaka Mitsuishi, and Koji Kimoto. Non-negative matrix factorization for mining big data obtained using four-dimensional scanning transmission electron microscopy. *Ultramicroscopy*, 221:113168, 2021.

Frances I Allen, Thomas C Pekin, Arun Persaud, Steven J Rozeveld, Gregory F Meyers, Jim Ciston, Colin Ophus, and Andrew M Minor. Fast grain mapping with sub-nanometer resolution using 4d-stem with grain classification by principal component analysis and non-negative matrix factorization. *Microscopy and microanalysis*, 27(4):794–803, 2021.

Koji Kimoto, Fumihiko Uesugi, Koji Harano, Jun Kikkawa, Ovidiu Cretu, Yuki Shibasaki, Motoki Shiga, and Atsushi Togo. Nonnegative matrix factorization incorporating domain specific constraints for four dimensional scanning transmission electron microscopy. *Scientific Reports*, 15(1):39143, 2025.

Koji Kimoto, Jun Kikkawa, Koji Harano, Ovidiu Cretu, Yuki Shibasaki, and Fumihiko Uesugi. Unsupervised machine learning combined with 4d scanning transmission electron microscopy for bimodal nanostructural analysis. *Scientific Reports*, 14(1):2901, 2024.

Wei Liu, Shengtong Zhang, Carolin B Wahl, Jiezhong Wu, Roberto Dos Reis, Chad A Mirkin, Vinayak P Dravid, Wei Chen, and Daniel W Apley. End-to-end automated segmentation framework for four-dimensional scanning transmission electron microscopy data. *Microscopy and Microanalysis*, 31(5):ozaf094, 2025.

Zhiqian Kho, Andy Bridger, Keith Butler, Ercin C Duran, Mohsen Danaie, and Alexander S Eggeman. On the use of clustering workflows for automated microstructure segmentation of analytical stem datasets. *APL Materials*, 13(1), 2025.

Kevin M Roccapriore, Ondrej Dyck, Mark P Oxley, Maxim Ziatdinov, and Sergei V Kalinin. Automated experiment in 4d-stem: exploring emergent physics and structural behaviors. *ACS nano*, 16(5):7605–7614, 2022.

Benjamin K Miller, Bernhard Schaffer, and Anahita Pakzad. Results before lunch: Capturing and processing in situ 5d stem, 2024.

Thomas C Pekin, Jun Ding, Christoph Gammer, Burak Ozdol, Colin Ophus, Mark Asta, Robert O Ritchie, and Andrew M Minor. Direct measurement of nanostructural change during in situ deformation of a bulk metallic glass. *Nature communications*, 10(1):2445, 2019.

Benjamin K Miller, Bernhard Schaffer, and Anahita Pakzad. Continuous 4d stem recording and visualization for in-situ experiments, 2023.

Bruno César da Silva, Zahra Sadre Montaz, Eva Monroy, Hanako Okuno, Jean-Luc Rouviere, David Cooper, and Martien Ilse Den Hertog. Assessment of active dopants and p–n junction abruptness using in situ biased 4d-stem. *Nano Letters*, 22(23): 9544–9550, 2022.

Robert Winkler, Alexander Zintler, Oscar Recalde-Benitez, Tianshu Jiang, Déspina Nasiou, Esmaeil Adabifiroozjaei, Philipp Schreyer, Taewook Kim, Eszter Piros, Nico Kaiser, et al. Texture transfer in dielectric layers via nanocrystalline networks: Insights from in situ 4d-stem. *Nano Letters*, 24(10):2998–3004, 2024.

Benjamin K Miller, Bernhard Schaffer, and Cory Czarnik. Real-time in-situ insights: Dynamic mapping with 4d stem. *Microscopy and Microanalysis*, 31(Supplement\_1):ozaf048–899, 2025a.

Min Chen, Karen C Bustillo, Yen Jea Lee, Colin Ophus, Jim Ciston, Brooks A Abel, Xi Jiang, Nitash P Balsara, and Andrew M Minor. In situ 4d-stem imaging of the orientation of lamellar clusters in polymer crystallization. *Macromolecular Rapid Communications*, page e00450, 2025.

Yongwen Sun, Ying Han, Dan Zhou, Hugo Perez Garza, Alejandro Gomez Perez, Thanos Galanis, Starvos Nicolopoulos, and Yang Yang. In-situ 4d-stem study of chemo-mechanical interactions during metal oxidation, 2024.

Benjamin K Miller, Liam Spillane, Emil Jensen, and Cory Czarnik. In-situ 4d stem: Capturing 5d insights into material dynamics in liquid. *Microscopy and Microanalysis*, 31(Supplement\_1):ozaf048–085, 2025b.

Ningyan Cheng, Hongyu Sun, Yevheniy Pivak, and Christian H Liebscher. Direct visualization and quantitative insights into the formation and phase evolution of cu nanoparticles via in situ liquid phase 4d-stem. *Advanced Science*, 12(19):2500706, 2025.

Matthew J Patrick, Sarah A Asher, Sylvia I Whang, Alan J Ma, Jeffrey M Rickman, and Katayun Barmak. In situ grain growth experiments: Tem imaging & automated segmentation with correlative 4d-stem orientation mapping. *Microscopy and Microanalysis*, 31(Supplement\_1):ozaf048–909, 2025.

Delphic Chen and Jui-Chao Kuo. Bilateral filter based orientation smoothing of ebsd data. *Ultramicroscopy*, 110(10):1297–1305, 2010.

Sandra Stangebye, Kunqing Ding, Yichen Yang, Ting Zhu, Olivier Pierron, and Josh Kacher. Grain size effects on stress-assisted grain boundary migration in polycrystalline au thin films under tension. *Acta Materialia*, page 121330, 2025.

Taylor J Woehl, James E Evans, Ilke Arslan, William D Ristenpart, and Nigel D Browning. Direct in situ determination of the mechanisms controlling nanoparticle nucleation and growth. *ACS nano*, 6(10):8599–8610, 2012.

Nicholas M Schneider, Michael M Norton, Brian J Mendel, Joseph M Grogan, Frances M Ross, and Haim H Bau. Electron–water interactions and implications for liquid cell electron microscopy. *The Journal of Physical Chemistry C*, 118(38):22373–22382, 2014.

Taylor J Woehl, Trevor Moser, James E Evans, and Frances M Ross. Electron-beam-driven chemical processes during liquid phase transmission electron microscopy. *MRS Bulletin*, 45(9):746–753, 2020.

Serin Lee, Nicholas M Schneider, Shu Fen Tan, and Frances M Ross. Temperature dependent nanochemistry and growth kinetics using liquid cell transmission electron microscopy. *ACS nano*, 17(6):5609–5619, 2023.

Birk Fritsch, Serin Lee, Andreas Körner, Nicholas M Schneider, Frances M Ross, and Andreas Hutzler. The influence of ionizing radiation on quantification for in situ and operando liquid-phase electron microscopy. *Advanced Materials*, 37(13):2415728, 2025.

Serin Lee, Tommy Watanabe, Frances M Ross, and Jeung Hun Park. Temperature dependent growth kinetics of pd nanocrystals: Insights from liquid cell transmission electron microscopy. *Small*, 20(51):2403969, 2024.

Daniel G Stroppa, Matthias Meffert, Christoph Hoermann, Pietro Zambon, Darya Bachevskaya, Hervé Remigy, Clemens Schulze-Briese, and Luca Piazza. From STEM to 4D STEM: Ultrafast diffraction mapping with a hybrid-pixel detector. *Microscopy Today*, 31(2):10–14, 2023.

Stefan Van der Walt, Johannes L Schönberger, Juan Nunez-Iglesias, François Boulogne, Joshua D Warner, Neil Yager, Emmanuel Gouillart, and Tony Yu. scikit-image: image processing in python. *PeerJ*, 2:e453, 2014.

Benjamin H Savitzky, Steven E Zeltmann, Lauren A Hughes, Hamish G Brown, Shiteng Zhao, Philipp M Pelz, Thomas C Pekin, Edward S Barnard, Jennifer Donohue, Luis Rangel DaCosta, et al. py4dstem: A software package for four-dimensional scanning transmission electron microscopy data analysis. *Microscopy and Microanalysis*, 27(4):712–743, 2021.

Stephanie M Ribet, Rohan Dhall, Colin Ophus, and Karen C Bustillo. Multi-angle precession electron diffraction (maped): a versatile approach to 4d-stem precession. *Microscopy and Microanalysis*, 31(6):ozaf103, 2025.

R Vincent and PA Midgley. Double conical beam-rocking system for measurement of integrated electron diffraction intensities. *Ultramicroscopy*, 53(3):271–282, 1994.

**Supplementary Material****Unsupervised clustering algorithm for efficient processing of 4D-STEM and 5D-STEM data**

Serin Lee<sup>1,\*</sup>, Stephanie M. Ribet<sup>2</sup>, Arthur R. C. McCray<sup>1</sup>, Andrew Barnum<sup>3</sup>, Jennifer A. Dionne<sup>1,\*</sup>, Colin Ophus<sup>1,\*</sup>

<sup>1</sup>Department of Materials Science and Engineering, Stanford University, Stanford, CA 94305, United States

<sup>2</sup>National Center for Electron Microscopy, Molecular Foundry, Lawrence Berkeley National Laboratory, Berkeley, CA 94720, United States

<sup>3</sup>Stanford Nano Shared Facilities, Stanford University, Stanford, CA 94305, United States

\*Corresponding authors: serinl@stanford.edu, jdionne@stanford.edu, cophus@stanford.edu

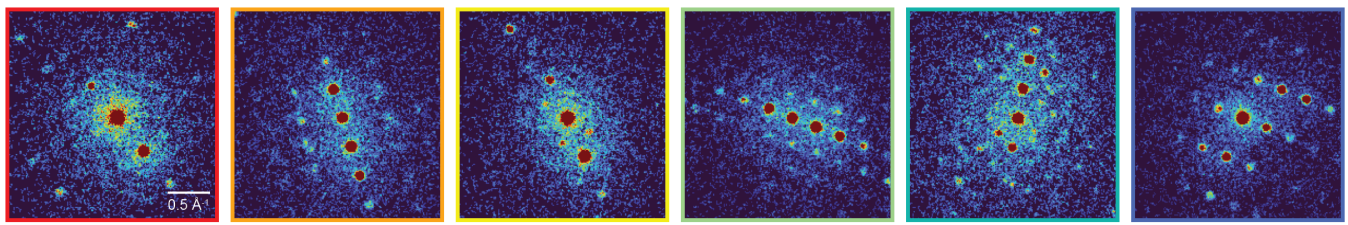


Fig. S1: Diffraction patterns of raw data without clustering and prefiltering. The color codes correspond to (Fig. 3)

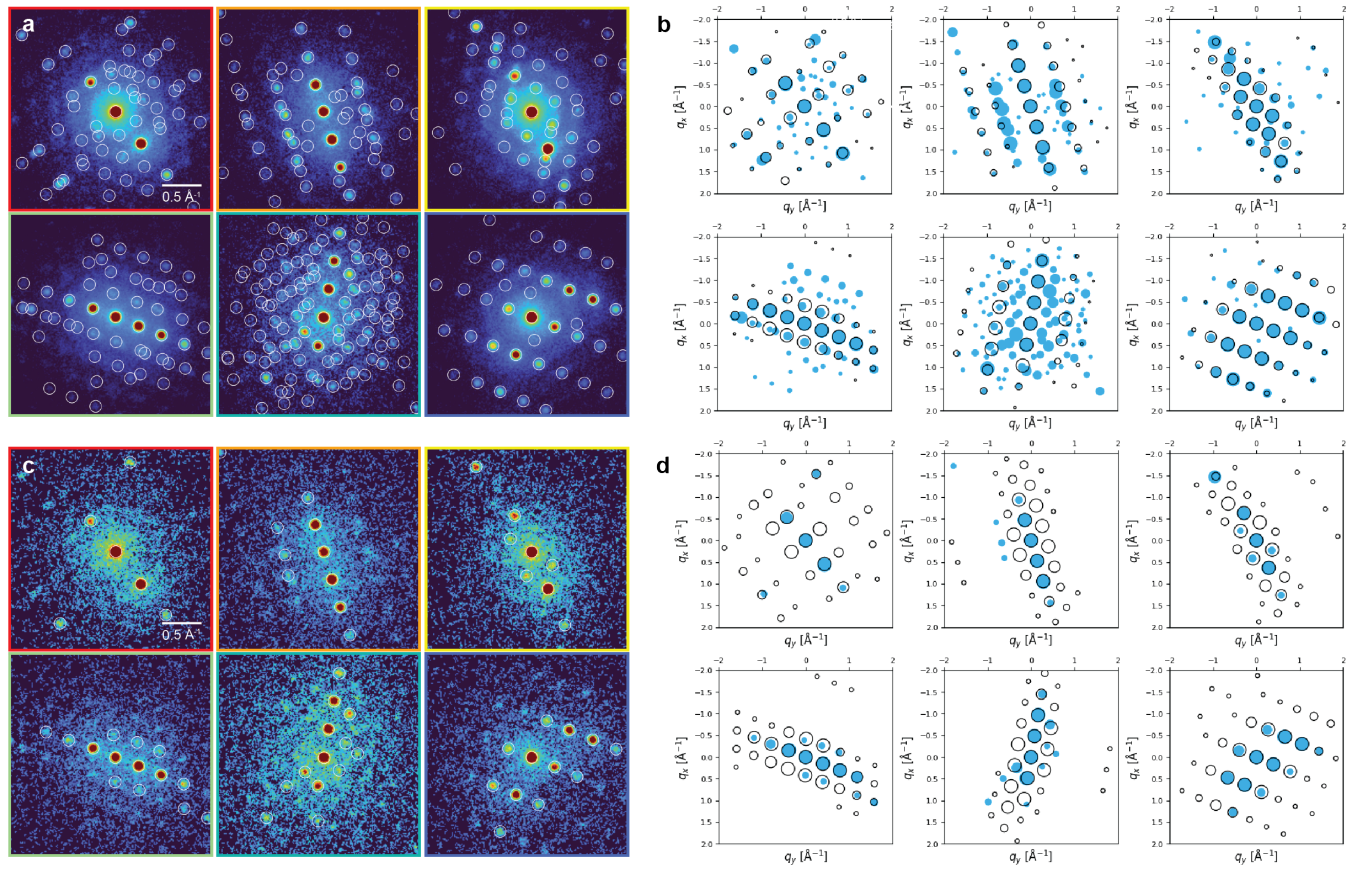


Fig. S2: Bragg disk detection and orientation mapping on diffraction patterns without clustering (a,b) and on raw data without clustering and prefiltering (c,d).